On the viability of chitosan-derived mesoporous carbons as supports for PtCu electrocatalysts in PEMFC

Julia Garcia-Cardona [a], Ignasi Sirés [a], Marco Mazzucato [b], Riccardo Brandiele [b], Enric Brillas [a], Francisco Alcaide [a,§], Christian Durante [b,*], Pere L. Cabot [a,*]

[a] *Laboratori d'Electroquímica dels Materials i del Medi Ambient, Departament de Química Física, Facultat de Química, Universitat de Barcelona, Martí i Franquès 1-11, Barcelona 08028, Spain*
[b] *Department of Chemical Sciences, University of Padua, Via Marzolo 1, Padova 35131, Italy*

ARTICLE INFO

ABSTRACT

Chitosan is an abundant and non-toxic natural polysaccharide rich in nitrogen, which is used here to obtain N-doped mesoporous carbons (NMCs) as supports for Pt-saving PtCu alloy elecrocatalysts, which can be of interest for low-temperature fuels cells. NMCs with different textural properties were synthesized from cheap silica templates. They presented relative dominance of disordered graphitic lattice and comparable amounts of pyrrolic and pyridinic N, with different specific BET surface areas (715–1040 m^2 g^{-1}) and mesopore (1.2–2.4 cm^3 g^{-1}) and micropore volumes (0.1–0.6 cm^3 g^{-1}). PtCu nanoparticles were deposited by Cu electroless deposition and further galvanic exchange with Pt, with overall Pt loadings about 20 wt.%. Pt-rich PtCu alloy crystallites with contracted Pt *fcc* lattices and sizes of 3.1–4.7 nm were formed. The synthesized PtCu/NMCs catalysts presented better specific current densities for the oxygen reduction and better CO tolerance and specific current densities for the methanol oxidation reaction than those of commercial Pt/C and PtCu/CMK-3. The PtCu/NMC prepared with the H_2SO_4–activated NMC was the most active catalyst. The different textural properties of the carbonaceous materials appeared to determine the surface structure of the PtCu nanoparticles.

1. Introduction

Platinum and Pt-based alloys, dispersed on a carbon support, are to date the best and most applied catalysts in proton exchange membrane (PEMFCs) and direct methanol fuel cells (DMFCs), which appear as promising power sources for electric vehicles and small instrumentation [1–3]. Catalyst and carbon support play together significant roles in the catalyst performance through their synergistic effects [4–7]. However, reducing their cost is necessary to plain the way to commercialization.

On one hand, Pt is expensive and scarce. Alloying with transition metals is interesting, not only in terms of cost (the Pt amount can thus be reduced), but also because of their electronic effect on Pt, which can improve its catalytic activity [8]. Thus, a wide variety of PtCu catalysts were synthesized in the past, mainly supported on carbon blacks Vulcan® XC-72 and XC-72R, which allowed increasing the catalytic activity toward the oxygen reduction, and the CO, methanol, and ethanol oxidation reactions [9–19].

On the other hand, the carbons supports should have high specific surface area, good conductivity, stability, and suitable porous structure facilitating the approach of the reactants and the products removal, as well as a good interaction between the support and the metallic nanoparticles (NPs) [7,20–25]. A wide variety of carbonaceous materials with different textures and surface structures, depending on the synthesis procedure, can be obtained. The most used and studied supports for fuel cell catalysts are carbon blacks such as Vulcan® XC-72 and XC-72R [9, 13,19,21], due to their low cost, high surface area, and good electrical conductivity. Nonetheless, they present some drawbacks such as deep micropores, which limit the accessibility of Nafion® and reactants to active sites, contain organo-sulphur impurities that can poison the catalyst, and can undergo corrosion while the cell operates [26,27]. For these reasons, alternative carbonaceous materials have been proposed [18,28–37]. It was shown that mesoporous carbons with high surface areas, adjustable pore structure and size, mechanical stability, and good conductivity, led to superior electrochemical and transport properties when compared to the traditional carbon materials [28,29-36,38]. Thus, improved catalytic activities of Pt and Pt-based NPs supported on

---

ordered mesoporous carbons (OMCs) such as CMK-3 were achieved [30-33,36]. Note however, that it is very difficult to synthesize mesoporous silica hard templates to promote carbon replicas with suitable pore size (> 10 nm) and, consequently, they are expensive [38–40]. For this reason, the authors used in the past very cheap silica P20 (SiO_2 NPs 10–20 nm in size), usually employed for chromatographic separation, as the template (porogen agent) to obtain supercapacitors from different carbon precursors [41]. On the other hand, the authors took profit from chitosan [42,43], a polysaccharide containing amine and hydroxyl groups, which is one of the most abundant natural organic compounds, present in crustacean shells [44]. It was used as precursor to synthesize N-doped mesoporous carbon (NMC) for H_2O_2 generation in water decontamination [42] and $Fe-N_x$ catalysts for the 4-electron O_2 reduction [43], thus making chitosan a chemical with added value from disposable biomass.

The object of this work was to synthesize novel carbon-supported Pt-saving PtCu catalysts by deposition of PtCu NPs on cheap mesoporous carbons, as a further step to the preparation of eco-friendly electrocatalysts, which can be of interest for low-temperature fuel cells. The strategy was to prepare carbons of different textural properties from chitosan as precursor, using different acid treatments to dissolve chitosan and P20 as silica template. Accordingly, the prepared carbons and supported PtCu were characterized by means of structural techniques, additionally testing the catalysts for the CO and methanol oxidation, and the oxygen reduction. The activity of the different catalysts against the reactions studied was compared to that obtained using commercial Pt/C and PtCu NPs dispersed on commercial ordered mesoporous carbon CMK-3.

2. Materials and methods

2.1. Chemicals

In the synthesis of the carbons, the following reagent grade chemicals were used: chitosan (CH), CH_3COONH_4, HCl (40 wt.%), ethylene glycol, CH_3COOH (glacial) and Nafion® (5 wt.% in a mixture of lower aliphatic alcohols and water), were from Sigma Aldrich; H_2SO_4 (96 wt. %), ethanol, and acetone, from Fluka; and isopropanol from Merck. Alpha Gaz O_2 and Ar were supplied by Air Liquid (>99.99%). The textural properties of the synthesized carbons were compared to those of CMK-3 mesoporous carbon from ACS Materials and to Vulcan® XC-72 carbon from Cabot Corp. For the electrochemical characterization, all the solutions were prepared using high-purity Milli-Q water (Merck purification system, resistivity > 18.2 MΩ cm at 25 ºC) and analytical-grade reagents. H_2SO_4 (96 wt.%) and $CuSO_4\bullet 5H_2O$ were supplied by Panreac-Applichem and n-heptane, poly(ethyleneglycol)-dodecyl ether (surfactant Brij-30) and $NaBH_4$, by Sigma-Aldrich. Catalyst cleaning solvents were ethanol (96 wt.%) and acetone (99.5 wt.%) purchased from Panreac. The Pt precursor was 8 wt.% aqueous solution of H_2PtCl_6 from Merck. For the electrochemical tests, Nafion® (5 wt.%) and dry isopropanol from Sigma-Aldrich were used for the ink preparation. The catalysts obtained were compared to commercial 20 wt.% Pt/C from Premetek, with XC-72 as the carbon support.

2.2. Synthesis of the carbon supports

The NMCs were synthesized using CH as the carbon precursor and silica P20 as the inorganic template. The same silica was utilized in previous work of the authors, although for different carbon precursors to be applied in supercapacitors [41]. As additional novelty, the effect of four different types of acids, H_2SO_4, CH_3COOH, HCl and CH_3COONH_4, was evaluated for prompting the chitosan dissolution in water, and the resulting carbons were accordingly named from CH1 to CH4. Note that HNO_3 was not used to avoid the formation of excessive oxygenated functional groups. In a typical synthesis, 3 g of CH were mixed with 1.5 g of silica P20 in 150 mL of water, then the solution was heated at 80 °C

for 3 h, and finally, after the addition of acid to the solution, the temperature was increased to 90 °C and kept for 12 h while stirring at a rotation speed of 500 rpm. Afterwards, the precursors powder was dried for 24 h and then placed in a tubular furnace and pyrolyzed using a two-step procedure. After the typical atmosphere conditioning, the powder was first heated in the furnace with a 75 sccm (standard cm^3 min^{-1}) N_2 flow at 100 °C for 1 h and, subsequently, the temperature was raised up to 750 °C at a rate of 5 °C min^{-1} and kept at that temperature for 2 h. The template was etched by treatment in a solution containing ethanol and NaOH at a concentration of 2 M in bath sonicator for 3 days, keeping the temperature under 35 °C. The carbon was then separated by vacuum filtration on a nylon nanometric filter and dried overnight.

2.3. Synthesis of the supported catalysts

The catalysts were synthesized by a water-in-oil method. The microemulsion consisted of n-heptane, Brij-30 and an aqueous solution of $CuSO_4$, with a water-to-surfactant molar ratio of 7:1 [45]. The reducing agent, $NaBH_4$, was slowly added to the magnetically stirred microemulsion to form the Cu nanoparticles, with a reductant-to-metal molar ratio of 9:1 and a total stirring time of 2 h. After the reductant removal, 0.5 mL of the 8 wt.% H_2PtCl_6 solution was slowly added to perform the galvanic exchange, keeping the magnetic stirring for 1 h. Finally, 21 mg of the carbon support were added to the microemulsion, also stirring for 1 h and then, acetone was added for the phase separation. Once the organic phase was clean, it was separated from the aqueous phase and the powder was filtered. Then, the powder was added to a 5 mM H_2PtCl_6 + 0.1 M $HClO_4$ solution to improve the galvanic replacement, sonicating the suspension in bath for 1 h. Finally, the suspension was filtered, and the catalyst powder cleaned with ethanol. The resulting powder was left to dry overnight at 80 ºC. The corresponding PtCu carbon-supported catalysts were then identified as PtCu/CH1, PtCu/CH2, PtCu/CH3, PtCu/CH4, and PtCu/CMK-3.

2.4. Structural characterization

The textural and physicochemical characteristics of the synthesized carbons were studied by transmission electron microscopy (TEM), elemental analyses (EA), N_2 absorption/desorption, Raman spectroscopy and X-ray photoelectron spectroscopy (XPS). TEM observations were performed using a FEI Tecnai G2 transmission electron microscope operating at 100 kV. EA was carried out using a Thermo Scientific Flash 2000 analyser. N_2 desorption/desorption isotherms were recorded at 77.3 K using a Micromeritics ASAP 2020 Plus instrument. The specific surface areas of the samples were calculated by multipoint Brunauer-Emmett-Teller (BET) analysis; the total pore volume was obtained by applying Gurvich law at $p/p^0 \sim 0.95$–1, whereas the t-plot method was used to measure the micropore volume. Pore size distribution curves were derived using density functional theory (DFT) methods and, finally, the number of mesopores was calculated as the difference between the total number of pores and the number of micropores. The Raman spectra were obtained using a DXR Raman microscope system from Thermo Fischer Scientific. The photoexcitation was performed using a laser of $\lambda = 532$ nm, a spot size on the sample ~ 25 μm and a power at the sample in the range 0.1–1.0 mW. The XPS measurements were performed at room temperature in an ultra-high vacuum (UHV) chamber (base pressure $< 5 \times 10^{-9}$ mbar), equipped with a double anode X-ray source (omicron DAR-400) and a hemispherical electron analyser (omicron EIS-125). A non-monochromatized Mg-K_α radiation ($h\nu = 1253.6$ eV) and pass energies of 50 and 20 eV for the survey and the single spectral windows, respectively, were used. The calibration of the binding energy (BE) scale was carried out using Au $4f^{7/2}$ as a reference (BE Au $4f^{7/2} = 84.0$ eV). The XPS peaks of carbon, oxygen and nitrogen were separated into single components by using symmetrical Voigt functions.

The catalysts prepared using the indicated supports were analysed

using X-ray diffraction (XRD) and TEM. For the XRD analyses, the samples were sandwiched between films of 3.6 μm – thick polyester (Mylar®), using a PANalytical X'Pert PRO MPD θ/θ powder diffractometer, with a Cu anode, 45 kV and 40 mA, Cu K$_\alpha$-filtered radiation (λ = 1.5418 Å), step size of 0.026° and measuring time of 200 s per step. The morphologies and overall composition of the catalysts were examined by means of 200 kV JEOL JEM 2100 transmission electrode microscope furnished with the energy-dispersive X-ray spectroscopy (EDS) technique. For the EDS analyses, different representative domains of the sample were analysed, and the mean values were taken as the corresponding overall compositions.

2.5. Electrochemical tests

The electrochemical activity measurements were carried out by cyclic voltammetry (CV) and linear sweep voltammetry (LSV) in a cell with a double wall for the temperature regulation (25 ± 0.1 °C) by means of Julabo MP-5 thermostat and a three-electrode setup, with a glassy carbon electrode (GCE) from Metrohm (0.196 cm^2 area) as the working one, a Pt wire as the auxiliary electrode and a reversible hydrogen electrode (RHE) from Gaskatel GmbH as the reference. All the potentials mentioned in this paper are referred to the latter. The GCE tip was coupled to a rotating disk electrode (RDE) from Metrohm Autolab B.V. The GCE was polished using a PSA-backed white felt cloth from Buehler containing Micropolish II deagglomerated alumina of 0.3 and 0.05 μm. The catalysts inks were prepared by dispersing 2 mg of the catalysts in 0.5 mL of ultrapure water by sonication for 30 min. Then, suitable amounts of the catalyst inks were deposited on the GCE tip using a micropipette and once dried at room temperature, the catalyst layer was coated with 2.5 μL of 1 wt.% Nafion®.

The electrolyte used for the experiments was deaerated 0.5 M H$_2$SO$_4$ and the measurements were performed using an Autolab PGSTAT100 potentiostat-galvanostat controlled by NOVA 2.1.4 software. The solution deaeration was performed before the electrochemical experiments by bubbling N$_2$ through the solution and during the measurements it was maintained over the liquid phase. The freshly prepared working electrodes were repetitively cycled at 100 mV s^{-1} in the potential range from 0.0 to 1.2 V to attain steady voltammograms. The successive voltammograms obtained during this repetitive cycling presented a slight increase in the hydrogen adsorption/desorption currents, which was related to the electrochemical cleaning. Once stabilized, the representative cyclic voltammograms were acquired at 20 mV s^{-1}.

The CO tolerance of the catalysts was tested by CO stripping. In this case, CO was bubbled for 15 min while keeping the electrode potential at 0.1 V and, afterwards, the CO dissolved was removed using N$_2$. Then the monolayer of preadsorbed CO was oxidized by CV at 20 mV s^{-1} between 0.0 and 1.2 V. The activity test towards the ORR was performed by LSV in an O$_2$-saturated (atmospheric pressure) 0.5 M H$_2$SO$_4$, scanning the potential from the open circuit potential to 0.2 V at a scan rate of 5 mV s^{-1}, rotating the GCE tip of the RDE at 1500 rpm. The activity towards the MOR was examined by CV at 20 mV s^{-1}, between 0.0 to 1.2 V, using deaerated 1.0 M solutions of the alcohol in 0.5 M H$_2$SO$_4$. The Pt loading in these ORR and MOR studies was set close to 20 μg$_{Pt}$ cm^{-2}.

3. Results and discussion

3.1. Characterization of the mesoporous carbons

The heteroatoms concentration in the four samples was evaluated by elemental analysis. Fig. 1 shows the results obtained for the synthesized
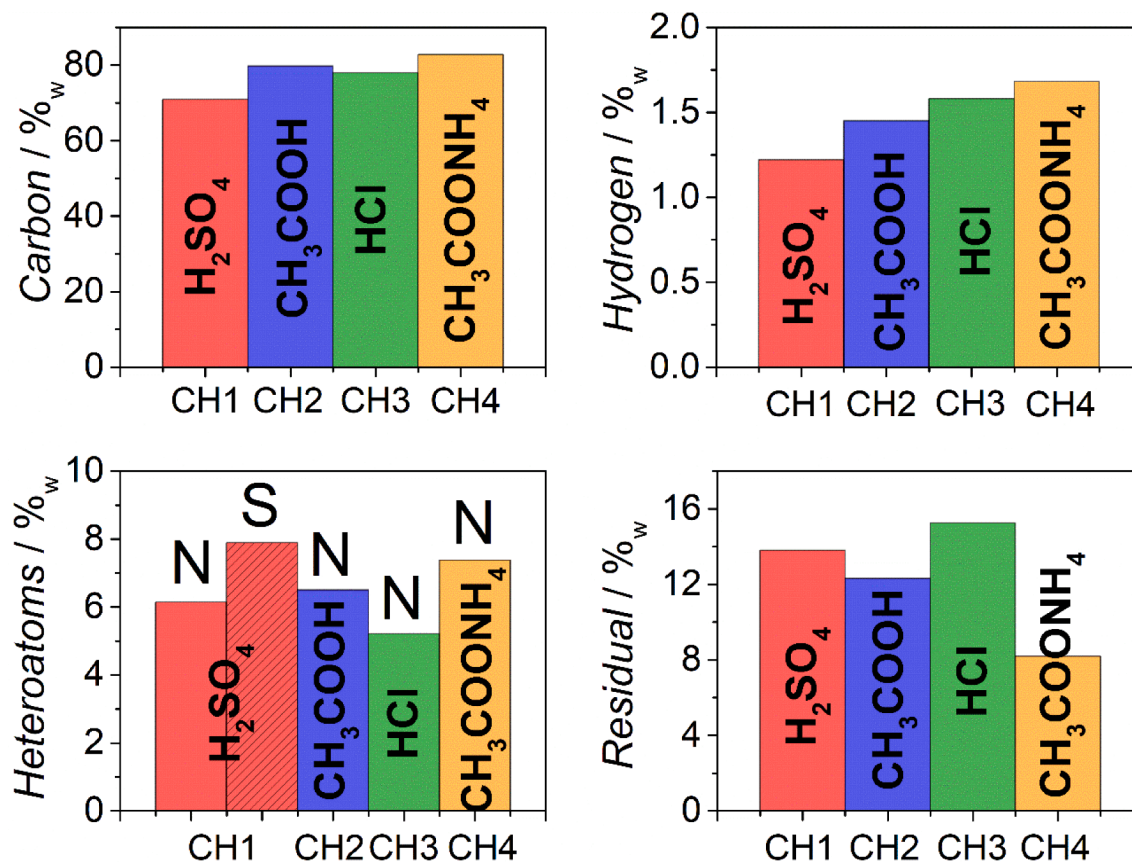

Fig. 1. Elemental analysis histograms.

NMCs. All the samples from CH1 to CH4 show an important nitrogen content ranging from 5.2 to 7.4 wt.%, the latter obtained when CH_3COONH_4 was employed for prompting the chitosan solubilization in water. The CH1 sample shows nitrogen-sulfur co-doping, where the sulfur source is the H_2SO_4 used for increasing the chitosan solubility during the impregnation process. In all the samples, the residual element corresponds to the oxygen, from 8.2 to 13.8 wt.%, meaning that a substantial functionalization with oxygen groups is attained, especially in the sample prepared by using strong acidic conditions (HCl and H_2SO_4).

The highly porous nature of CH carbons was revealed by TEM measurements, which show the presence of carbon flakes characterized by round shape mesopores, all with diameters between 15 and 20 nm. TEM images of Fig. S1 in the Supporting Information (SI) file show the formation of an interconnected porous structure, which is the result of the interconnection of quasi-round pores created by the imprinting action of the SiO_2 NPs.

The synthesized NMCs showed a high specific BET surface area (S_{tot}): 714.6, 872.3, 1041 and 1037 $m^2\ g^{-1}$ for CH1 to CH4, respectively. It is evident that the resulting S_{tot} is sensitive to the different acids used for increasing the chitosan solubility in water, which in turn affects the disposition of chitosan chain around the P20 particles. These values are greater than that measured for commercial CMK-3 (Table S1 and Fig. S2 in SI) and significantly greater than that obtained for commercial Vulcan® XC-72 (Table S1 and Fig. S3 in SI).

Fig. 2 shows the total pore, micropore and mesopore volumes: all the samples showed a larger volume of mesopores (V_{meso}) as compared to that of micropores (V_μ). This is especially evident when H_2SO_4 was employed as acid ($V_{meso} = 2.408\ m^2\ g^{-1}$ and $V_\mu = 0.108\ m^2\ g^{-1}$), but V_{meso} tended to decrease and V_μ tended to increase upon transition from CH1 to CH4. Note that as V_μ increased, V_{meso} decreased together with the total pore volume ($V_{tot} = V_\mu + V_{meso}$). Thus, V_{meso}/V_μ ratio was 22.7, 21.7, 6.1 and 1.9 for CH1, CH2, CH3 and CH4, respectively. The higher microporosity of CH3 and CH4 agrees with their larger BET area measured, greater than 1000 $m^2\ g^{-1}$. On the other hand, CMK-3 presented V_{tot}, V_{meso} and V_μ values of 0.923, 0.638 and 0.142 $cm^3\ g^{-1}$, respectively, whereas the values for Vulcan® XC-72 were 0.629, 0.260 and 0.055 $cm^3\ g^{-1}$, respectively, with the corresponding V_{meso}/V_μ ratios of 4.5 and 4.7 for CMK-3 and XC-72, respectively (Table S1 in the SI).

The graphitization degree of the CH-derived carbonaceous materials was evaluated by means of Raman spectroscopy. The spectra of all these mesoporous carbons were similar and have been exemplified in Fig. 3. As shown in this figure, these carbons did not present defined second-order Raman spectra (2400−2700 cm^{-1} region), and only a smeared flat band was present, which overlapped with the background noise. The spectra of all the CH1-CH4 carbons could be deconvoluted in the first-order region between 1100 and 1700 cm^{-1} by using four Gaussian bands, being D1, D3, D4 and G, corresponding to disordered graphitic lattice (D1 and D4), amorphous carbon (D3) and ideal graphitic lattice
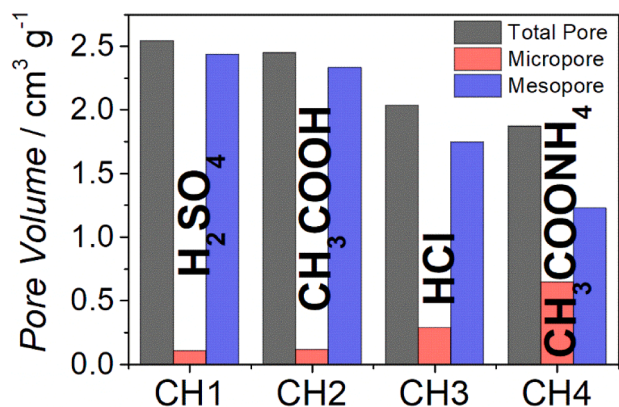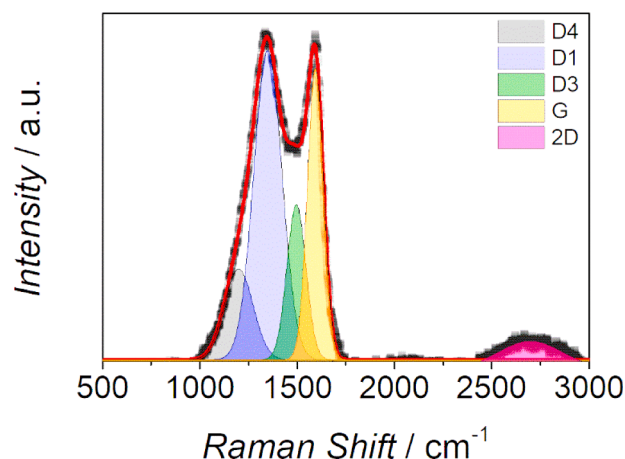

Fig. 3. Raman spectrum for mesoporous carbon CH3.

(G) [46]. D2, corresponding also to disordered graphitic lattice, has been also sometimes used, and it is generally located at 1620 cm^{-1}. However, it was not considered in the present case because a very good fitting of the experimental data was already obtained, even by keeping a minimum number of gaussian components. Note that the position of the main bands D1 and G did not significantly change when comparing the four NMCs, thus evidencing a very similar graphitization degree and content of amorphous carbon. In Fig. 3, the ratios of the peak areas corresponding to the different spectral bands with respect to that of the G band were determined as: $A_{D1}/A_G = 1.85$, $A_{D3}/A_G = 0.62$, $A_{D4}/A_G = 0.55$ and $A_{2D}/A_G = 0.38$.

An index that can be used for evaluating the degree of organization in carbon materials is *R2*, which can be calculated using Equation (1) [43,47]:

$$R2 = A_{D1} / (A_{D1} + A_G + A_{D2}) \tag{1}$$

where A_i is the area of the corresponding deconvolution peak and A_{D2} was considered to be equal to zero. Values of *R2* lower or greater than 0.5 are then indicative of the presence of lower or higher amounts of defective graphitic lattice in the carbonaceous material, respectively. The values of *R2* for the different CH-derived carbons did not substantially change, ranging between 0.55 and 0.65, which denoted the relative dominance of disordered graphitic lattice in these mesoporous materials.

The surface compositions of the synthesized carbons were analysed by XPS. They showed the presence of surface of oxygen, carbon and nitrogen and the absence of silica. The C 1 s biding energy (*BE*) region of CH3 presented a broad peak (Fig. 4a), which could be fitted with five main components, assigned to C sp^2 (C−C, *BE* = 284.4 eV), C sp^3 species bond to N (C−N, *BE* = 286.1 eV), C−O−C groups at 287.5 eV, carboxylic carbon (COOH, *BE* = 289.3 eV) and carbonate groups (CO_3^{2-}, *BE* = 290.8 eV) [48]. The same deconvolution was performed for all the synthesized carbons, with the exception that no significant carbonate peak was ascertained for CH1. As expected, the XPS spectrum of CH1 showed a S 2p peak, absent in the other CH-derived carbons, which could be assigned to one singular S-thiophene species (C − S − C, *BE* = 163.6 eV) [40,49].

The high-resolution XPS spectra in the N 1 s region of CH3 is depicted in Fig. 4b, where two main contributions could be deconvoluted, corresponding to pyrrolic and pyridinic nitrogen, as indicated. The relative peak areas corresponding to the different chemical species of C and N for the synthesized carbons have been collected in Table 1. It is worth mentioning the higher amount of the C sp^2 species and the dominance of pyrrolic N in CH2, CH3 and CH4 when compared to CH1.

The presence of pyridinic and/or pyrrolic N in these carbons is of additional interest, since a strong interaction between N and Pt may
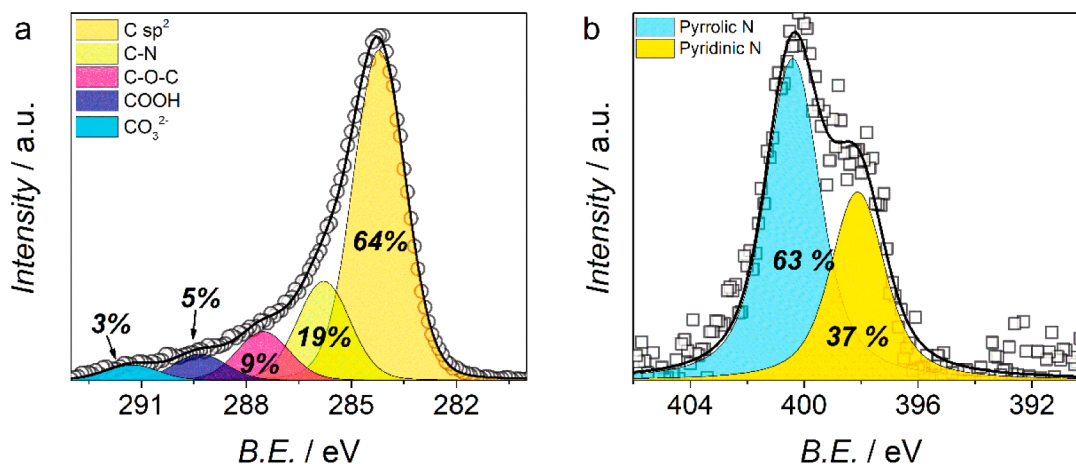

Fig. 2. Histogram for the pore volume of the four synthesized carbons.

Fig. 4. High-resolution XPS analyses of mesoporous carbon CH3 in the *BE* region of (a) carbon and (b) nitrogen. Hollow symbols (○ and □) correspond to the experimental data and the solid lines to fitting after deconvolution in the indicated bands.

result in excellent catalytic activity toward the ORR, as shown previously by dispersing Pt NPs on N-functionalized commercial mesoporous carbons [38].

It is then shown that inexpensive mesoporous carbons with variable mesoporosity to microporosity ratio can be obtained from an abundant precursor in disposable biomass, chitosan, modulated by the precursor treatment in different acids, with the help of cheap P20 hard templating silica. The obtained carbons, apart from oxygenated functional groups, presented pyridinic and pyrrolic N, which can operate as active sites for the catalyst anchoring.

3.2. Structural characteristics of the catalysts

Fig. 5a shows the XRD diffractograms of the different PtCu/NMCs, which are compared to PtCu/CMK-3 and Pt/C. All the diffractograms have a similar shape in which the dominance of the *fcc* Pt peaks is clear. However, the Pt-like XRD peaks for the PtCu samples show a slight shift with respect to those of Pt/C, what is better observed in the magnification shown in Fig. 5b.

The absence of peaks corresponding to Cu crystalline structures means that, if there were pure Cu or oxidized Cu crystallites, they had no sufficient size to be detected or they should be amorphous. The peaks at 2θ of 40.0, 46.3 and 67.5° correspond to (111), (200) and (220) *fcc* Pt planes, respectively [50]. In Fig. 5b, the (111) and (200) *fcc* Cu peaks have been marked, corresponding to 2θ angles of 43.3 and 50.5°, showing that those of PtCu fall between the peaks of pure Pt and pure Cu, although displaced toward the Pt peaks. These peak shifts strongly support the formation of PtCu alloy crystallites, since the Cu atomic radius (145 pm) is smaller than that of Pt (177 pm).

The composition of the PtCu alloys shown by these XRD analyses was estimated through Vegard's law, Eq. (2), which relates the lattice parameter of the PtCu alloy (a_{PtCu}) to the atomic fraction of Cu (x) and the lattice parameters of pure Pt ($a_{Pt} = 0.3916$ nm) and Cu ($a_{Cu} = 0.3608$ nm) [50]:

$$a_{PtCu} = (1-x)a_{Pt} + xa_{Cu} \qquad (2)$$

The Pt:Cu atomic ratios, collected in Table 2, show that the PtCu alloy crystallites formed are Pt-rich, with Pt amounts 5–9 times higher than Cu. The alloy formation indicates that in the galvanic replacement that takes place in the presence of Pt(IV), Cu is oxidized and replaced by Pt with some lattice reordering, which results in a PtCu alloy, in agreement with previous literature [18,13,51]. Note, however, that the peak broadness shown in Fig. 5 can be due to a small crystallite size and also to a peak superposition of phases having slightly different compositions [52]. For this reason, the alloy composition measured should be regarded as a mean value.

Despite not being pure metals, the crystallite sizes *d* can be estimated using Scherrer's equation:

$$d = \frac{K\lambda}{B\cos\theta} \qquad (3)$$

where $K = 0.9$, λ is the wavelength of the X-ray radiation, and *B* is the width of the peak (in radians) at half the maximum intensity The mean crystallite sizes obtained were around 3–4 nm (Table 2), slightly higher than that of the Pt nanoparticles in commercial Pt/C, but they can also be considered useful for fuel cell applications.

The PtCu/NMCs catalysts were also examined by TEM and compared to PtCu/CMK-3 and Pt/C (Fig. 6). According to the corresponding images, the PtCu NPs presented a rather spherical form, with sizes consistent with those estimated from XRD (Table 2). There is clear evidence of the successful attachment of the nanoparticles to the carbon supports, displaying some aggregation. However, the distribution and aggregation of the nanoparticles appear to be affected by the texture of the support. The corresponding EDS analyses provided the metallic overall compositions, also included in Table 2. Note that all the PtCu catalysts presented similar Pt contents in the range 22–33 wt.%, comparable to that of Pt/C, with Cu contents in the range 14–21 wt.%. The overall amounts of Pt and Cu did not vary too much from one catalyst to another, what is not strange because they were prepared in the same way. It is important to note, however, that the overall Pt:Cu atomic ratios in the catalyst were in the range 30–40 at.% Pt and 60–70 at.% Cu, which are very different from the alloy composition identified by XRD. Similar results were obtained by us when using CMK-3 and other supports, although with different synthesis procedure [18,36]. This can be explained considering that the composition of the crystallites obtained from XRD refers to the Pt and Cu zero-valent elements and by the presence of significant amounts of Cu oxidized species on the carbon surface, resulting from the galvanic exchange. It was shown that the latter were easily removed by Ar$^+$ sputtering in the XPS analyses, and it

Table 1
Relative atomic composition (%) of the different oxidation states of C and N, obtained from the corresponding XPS high-resolution spectra.

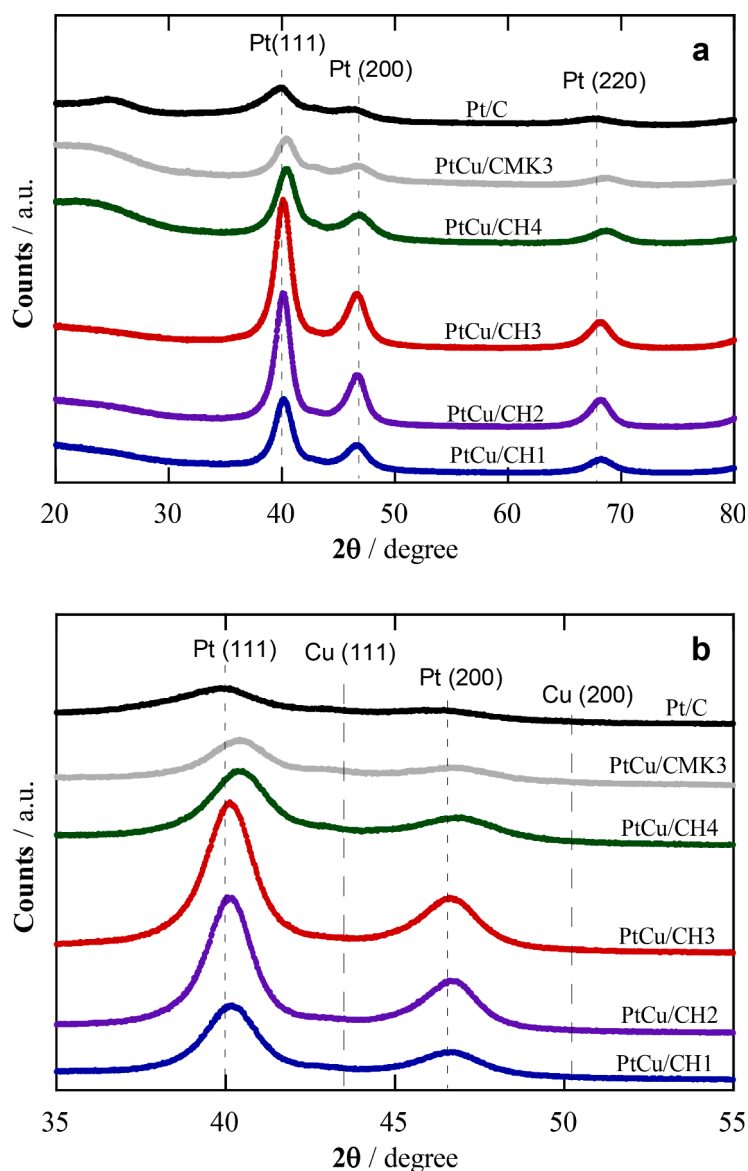| Mesoporous carbon	C sp^2	C–N	COOH	C–O–C	CO$_3^{2-}$	Pyrrolic N	Pyridinic N
CH1	52	24	7	17	0	48	52
CH2	70	16	4	6	4	61	39
CH3	64	19	5	9	3	63	37
CH4	68	17	5	8	3	60	40

Fig. 5. XRD diffractograms of (a) the PtCu supported catalysts and (b) magnification of the main peaks observed, which correspond to Pt (111) and (200) plains.

Table 2
Metallic composition and crystallite size of the PtCu alloys identified by XRD (see Fig. 5), and overall metal contents of the catalysts measured from the EDS analyses.

Catalyst	Pt:Cu at.%	Crystallite size / nm	Metal content[a] / wt.%	
			Pt	Cu
PtCu/CH1	83:17	3.1	26	16
PtCu/CH2	87:13	4.7	26	20
PtCu/CH3	90:10	4.2	33	21
PtCu/CH4	84:16	3.3	22	18
PtCu/CMK-3	98:2	3.2	25	14
Pt/C	100:0	2.6	19	-

[a] Mean standard deviation of 2 wt.%.

is also expected that they should be also dissolved in the acidic electrolyte and electrochemical cleaning before the electrochemical tests.

These results show that the PtCu alloy nanoparticles, about 4 nm in size, were successfully attached to the mesoporous carbon supports, with some aggregation and composition dependence on the textural properties of the latter.

3.3. Electrochemical tests

The cyclic voltammograms of the PtCu/NMCs were first obtained in deaerated 0.5 M H_2SO_4 at 20 mV s^{-1} to examine the hydrogen adsorption/desorption peaks. The steady cyclic voltammograms obtained after electrochemical cleaning for representative PtCu/NMCs catalysts are shown in Fig. 7a. They have been compared to commercial Pt/C after normalizing to the respective mean value of the hydrogen adsorption and desorption charges, which are proportional to the number of active sites. Three distinct potential regions can be observed in all the cyclic voltammograms of the PtCu/NMCs, which match to those of commercial Pt/C: *i*) the hydrogen adsorption/desorption region (0.0–0.3 V), from which the coulombic charge of H adsorption and desorption (Q_H) can be obtained to estimate the electrochemical active surface area; *ii*) the pseudocapacitive region (0.3–0.7 V), which is proportional to the specific surface area of the carbon support; and *iii*) the oxidation/reduction of the surface Pt/PtO couple around 0.80 V (Pt oxidation from 0.80 V in the anodic sweep with the corresponding PtO reduction peak potential in the cathodic sweep at about 0.75 V). Note that the currents corresponding to the pseudocapacitive region for the PtCu/NMCs are higher than those of commercial Pt/C. This can be explained by the different
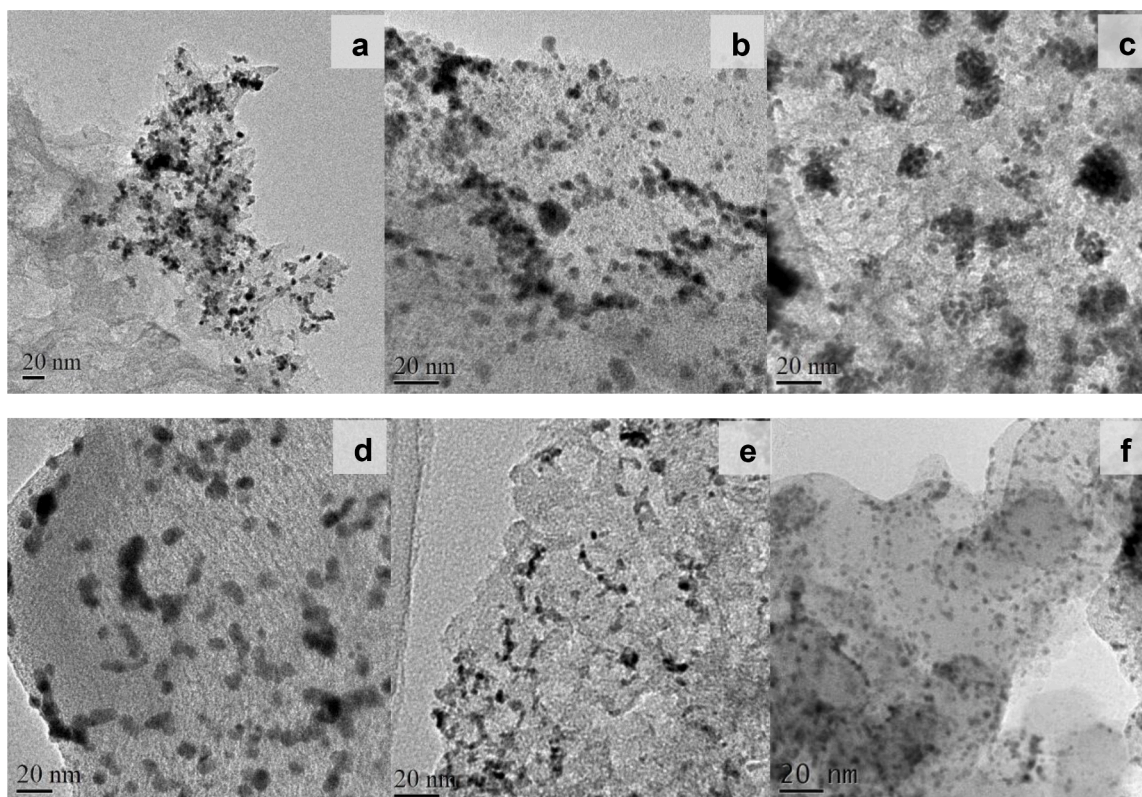
Fig. 6. TEM micrographs of the different specimens studied: (a) PtCu/CH1, (b) PtCu/CH2, (c) PtCu/CH3, (d)PtCu/CH4, (e) PtCu/CMK-3 and (f) commercial Pt/C.

specific total surface areas of the different carbons, which is of 223 m^2 g^{-1} for commercial Vulcan® XC-72 (Table S2 in SI), whereas they are over three-times greater for the mesoporous carbons of this work, as indicated above. Any evidence about Cu oxidation peaks in the cyclic voltammograms of the PtCu/NMCs was obtained, thus indicating the dominance of Pt on the PtCu surface NPs, achieved by the galvanic replacement and further CV cleaning [18,36]. Note in addition that the adsorption/desorption peaks of hydrogen in the PtCu/NMCs were not as well defined as those on Pt/C, most probably due to the Cu alloying, which can condition the Pt structural ordering on the surface of the nanoparticles [9,18].

The cyclic voltammograms of the CO stripping experiments have been depicted in Fig. 7b, where the oxidation of the CO monolayer that was previously adsorbed appear as the peak in the anodic sweep in the potential range between 0.6 and 1.0 V, although the onset and peak potentials depend on the catalyst. Note also that these curves have been normalized to the corresponding CO stripping charges for a better comparison, because these charges are proportional to the number of Pt active sites in each specimen.

It can be observed in the voltammograms shown in Fig. 7b that the stripping peaks for the PtCu/NMCs are shifted to more negative potentials than that corresponding to Pt/C. As shown in this figure, the onset potentials for the CO oxidation were about 0.70 V for the latter and about 0.65 V for the former, in agreement with previous results of the authors using PtCu NPs obtained also by galvanic exchange, although for different carbon supports [18,36]. This shift in the negative direction indicates improved activity toward CO oxidation (i.e., better CO tolerance), and can be explained by the electronic effects of Cu on Pt, which combine the compressive strain of the Pt lattice due to the smaller size of Cu (geometric effect) and the electron-donation of Cu on Pt due to the smaller electronegativity of the former (ligand effect), eventually weakening the CO bond and allowing its easier removal [9,18,36,53].

The electrochemical active surface area *ECSA* of each specimen was obtained from the hydrogen adsorption/desorption charges ($ECSA_H$) and from CO stripping ($ECSA_{CO}$), according to the following equations:

$$ECSA_H = \frac{Q_H}{210 \cdot m_{Pt}} \tag{4}$$

$$ECSA_{CO} = \frac{Q_{CO}}{420 \cdot m_{Pt}} \tag{5}$$

where Q_H and Q_{CO} are, respectively, the mean charge involved in the hydrogen adsorption/desorption and in the CO stripping charge (μC), m_{Pt} is the load of Pt (g) on the GCE, and 210 and 420 are the charges (μC cm^{-2}) associated to the oxidation of a monolayer of adsorbed H atoms (one-electron) and CO molecules (two-electron), also, respectively [54]. The *ECSA* values of the catalysts have been summarized in Table 3, showing a good agreement between those obtained from the hydrogen adsorption/desorption and CO stripping. Except for PtCu/CH4, they are in the range 15–22 m^2 g_{Pt}^{-1}, being smaller than for Pt/C. These rather low values can be explained, apart from the abovementioned larger nano-particle size of PtCu/NMCs (Table 3), by the agglomeration of the PtCu NPs, which could reduce the number of accessible Pt active sites. This is in agreement with the TEM pictures shown in Fig. 6, in which more aggregation for CH3 is appreciated when compared to CH2. This is apparently related to the carbon microporosity. In fact, the micro-porosity of CH1 and CH2 is low and comparable (V_{meso}/V_μ ratios of 22.7 and 21.7), whereas it is significantly higher for CH3 and CH4 (V_{meso}/V_μ ratios 6.1 and 1.9). Accordingly, the *ECSAs* of CH1 and CH2 are com-parable, and decreased when moving from CH2 to CH4. The higher microporosity of CH3 and CH4 allowed increasing their specific surface area, but could stimulate the nanoparticles aggregation.

The linear sweep voltammograms to study the ORR performance of the different catalysts in O_2-saturated 0.5 M H_2SO_4 solution at 5 mV s^{-1}
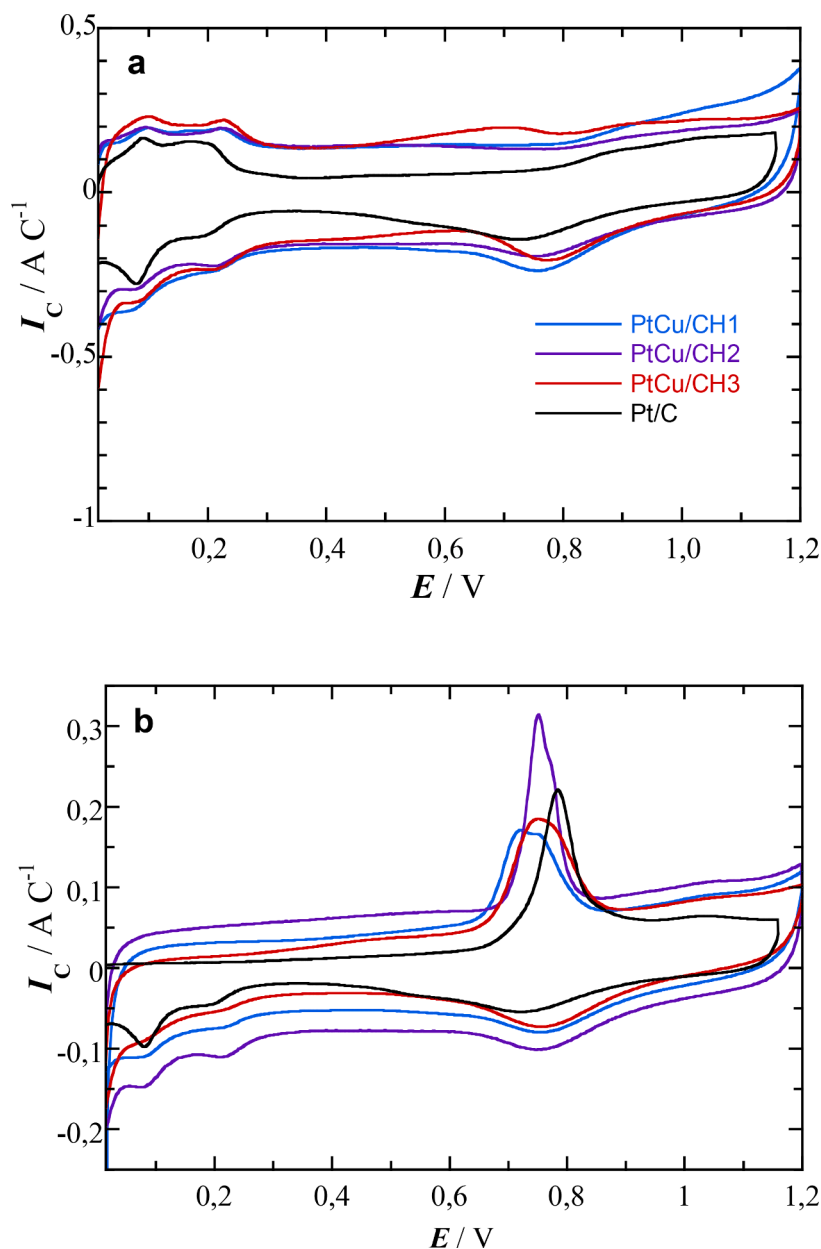
Fig. 7. (a) Cyclic voltammograms of the indicated PtCu/NMCs catalysts and (b) CO stripping curves of the same catalysts as in (a), compared to commercial Pt/C. Obtained in deaerated 0.5 M H_2SO_4 at a scan rate of 20 mV s^{-1}.

Table 3

ECSAs measured from the hydrogen adsorption/desorption (H) and from the CO stripping (CO) charges in the corresponding cyclic voltammograms.

Catalyst	Pt loading/ μg cm^{-2}	$ECSA_H$/ m^2 g_{Pt}^{-1}	$ECSA_{CO}$/ m^2 g_{Pt}^{-1}
PtCu/CH1	22.3	21.4	21.7
PtCu/CH2	22.4	21.7	21.8
PtCu/CH3	24.7	16.2	16.9
PtCu/CH4	23.5	9.5	9.7
PtCu/CMK-3	21.4	15.6	15.7
Pt/C	20.4	84.3	85.2

and an RDE rotation rate of 1500 rpm, are shown in Fig. 8. Fig. 8a refers to the Pt mass (mass activity, j_m) and shows single waves in all cases, with limiting currents depending on the catalyst. When referred to the electrode section, the limiting current densities were comparable and about 2.5–3 mA cm^{-2} (see Fig. S4 in the SI file), except for PtCu/CH4 and PtCu/CMK-3, which were somewhat smaller. As shown in Fig. 8a,

the Pt/C mass activity is the highest, which is an expected result, since its *ECSA* is about four times greater than those of PtCu/NMCs and PtCu/CMK-3, with about the same Pt loading. If, conversely, comparison is made in terms of current per *ECSA* (specific activities, j_{sp} in Fig. 8b), it is now the Pt/C that exhibits the smallest values. As the specific activities give the activity per unit of active area, higher values indicate greater catalytic activity and thus, all the PtCu catalysts appear to be more active than Pt/C.

The better activity of the PtCu/NMCs for ORR agrees with the CO stripping results of Fig. 7b, in which Cu alloying makes Pt more active in front of the CO oxidation and can also be explained by the electronic effects of Cu on Pt. As a method to quantify this specific activity, the potentials to attain a given j_{sp} were determined in the Tafel region of the ORR (E_{onset} and $E_{0.1}$ at −0.01 and −0.1 mA cm_{Pt}^{-2}, respectively) and the j_{sp} values at 0.9 V (-$j_{sp(0.9V)}$) were additionally considered. These data have been listed in Table 4, revealing a clear advantage of PtCu/CH3, with E_{onset} and $E_{0.1}$ values about 45 mV more positive than those of Pt/C,
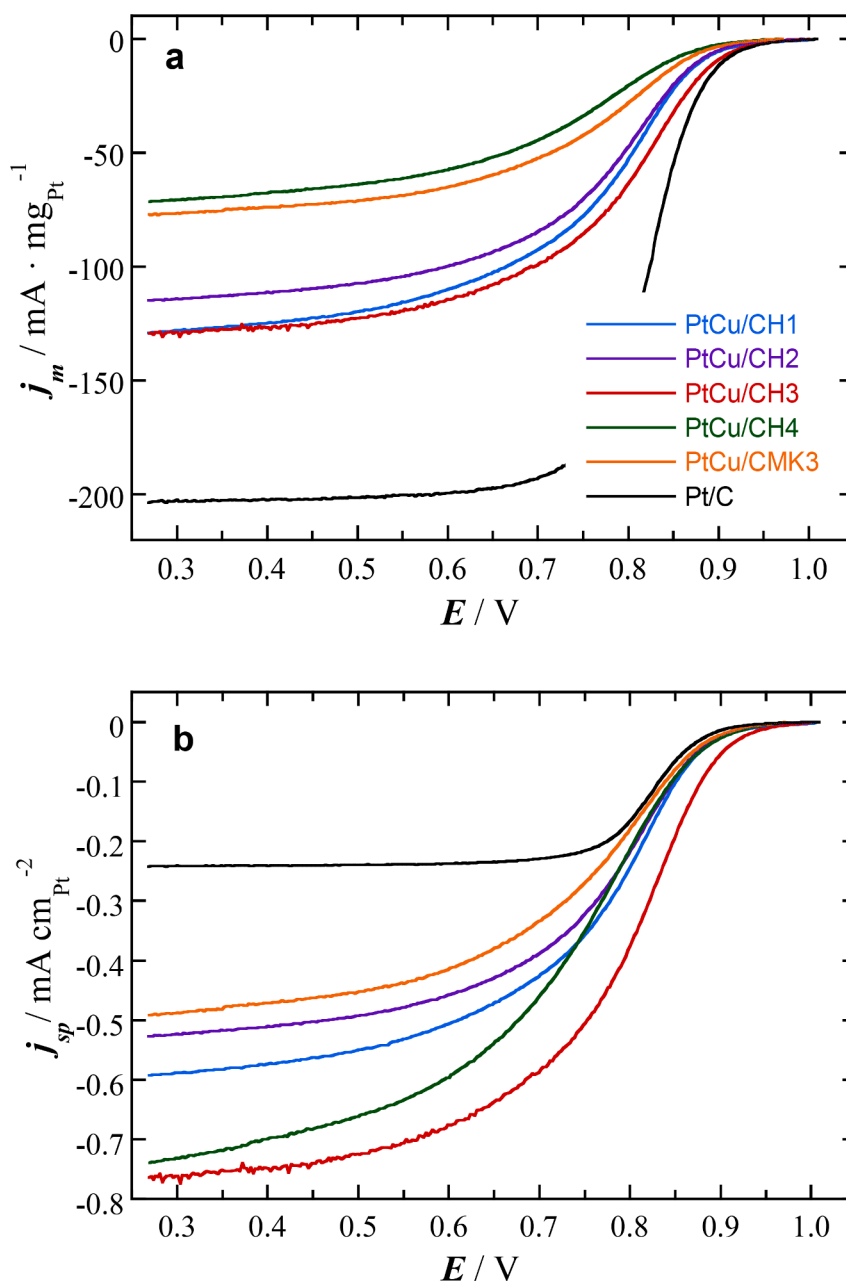
Fig. 8. Linear sweep voltammograms at 5 mV s^{-1} for the ORR in O$_2$-saturated 0.50 M H$_2$SO$_4$, the current densities being referred to the (a) Pt mass (j_m, mass activity) and (b) *ECSA* (j_{sp}, specific activity). RDE rotation rate of 1500 rpm.

also with the highest j_{sp} at 0.9 V. The other PtCu/NMCs present intermediate values between both and again, the PtCu/NMCs exhibit better catalytic activity than commercial Pt/C. Note in addition that better

ORR results have been obtained using the present NMCs as compared to commercial CMK-3. In the case of the RDE experiments, the limiting currents referred to the electrode section are not expected to significantly depend on the carbon porosity. However, the carbon porosity can be responsible for the dispersion of the PtCu NPs and their accessibility to the Pt(IV) species in the further galvanic exchange. Evidence about this point is that the composition of the crystallites depended on the support (see Table 2), that corresponding to PtCu/CH3 having the smallest Cu content (10 at.%) in the synthesized NMCs. In the case of PtCu/CMK-3, the Cu content of the crystallites was too small (2 at.%) and presented the lowest activity toward the ORR. It has been shown that building up a suitable structure of the PtCu surface is essential for a good catalytic performance and that an excessive Cu content of the PtCu crystallites was not suitable [55,56]. Therefore, it is interpreted that the final composition and surface structure of the PtCu nanoparticles was conditioned by the different textural properties of the NMCs.

Table 4
Catalytic activity data obtained from LSV for the ORR using the RDE at 1500 rpm and for the MOR without rotation.

Catalyst	ORR			MOR	
	E_{onset} / mV	$E_{0.1}$ / mV	-$j_{sp(0.9V)}$ / mA cm$_{Pt}^{-2}$	$E_{0.1}$ (mV)	j_f / j_r
PtCu/CH1	934	850	26	660	1.4
PtCu/CH2	926	847	23	644	1.2
PtCu/CH3	952	878	54	644	1.1
PtCu/CH4	932	846	27	658	1.2
PtCu/CMK-3	925	839	22	727	1.8
Pt/C	909	832	14	700	0.9

The cyclic voltammograms in deaerated 1.0 M MeOH + 0.5 M H_2SO_4 to study the MOR showed the same profile (Fig. S5 in SI), with an initial current growth leading to a forward peak (*f*) and a reverse one (*r*), with respective peak current densities j_f and j_r. As examples, Fig. S5a in the SI file shows the CV profile for PtCu/CH3 and Fig. S5b that of Pt/C. The j_f/j_r ratio has been taken in previous reports as a measure of the catalyst poisoning by the intermediates generated during the MeOH oxidation, the oxidation of such intermediates being easier in the forward scan as the j_f/j_r ratio increases [57]. As shown in Fig. S5 and Table 4, $j_f > j_r$ for all the PtCu catalysts and, conversely, $j_f < j_r$ for commercial Pt/C. However, this interpretation has been criticized sometimes because in situ surface-enhanced infrared measurements during the methanol oxidation on Pt showed that the forward and backward peaks shared the same origin, i.e. the oxidation of freshly chemisorbed $MeOH_{ads}$ species [37, 58]. Normalization with respect to the Pt mass and/or to the *ECSA* was then suggested as the best way of comparing the corresponding catalysts activities. This is done in Fig. 9, which compares the linear sweep voltammograms for the MOR considering the mass (j_m) and specific activities (j_{sp}).

It is shown in Fig. 9a that the mass activities of PtCu/CH2 and PtCu/CH3 competed with those of commercial Pt/C. Note, however, that this may arise from the smaller size and lower aggregation of the Pt NPs in the latter, since according to the data listed in Table 3 and despite using the same Pt loading on the GCE, the *ECSAs* of the PtCu/NMCs were about four times smaller. Therefore, the catalytic activities would be better represented by the specific values referred to the *ECSAs* j_{sp}, shown in Fig. 9b. For this comparison, the potentials corresponding to a $j_{sp} = 0.1$ mA cm^{-2} ($E_{0.1}$) were selected as representative of the activity of the different catalysts, those being less positive presenting a smaller overpotential and thus, a higher activity. These results are also listed in Table 4, where it is shown that the best values were obtained for PtCu/CH3, which were 56 mV more negative than that of Pt/C. The highest specific current density was also obtained for PtCu/CH3, with a value of 1.2 mA cm^{-2} at a peak potential of 0.90 V. The PtCu catalysts are more
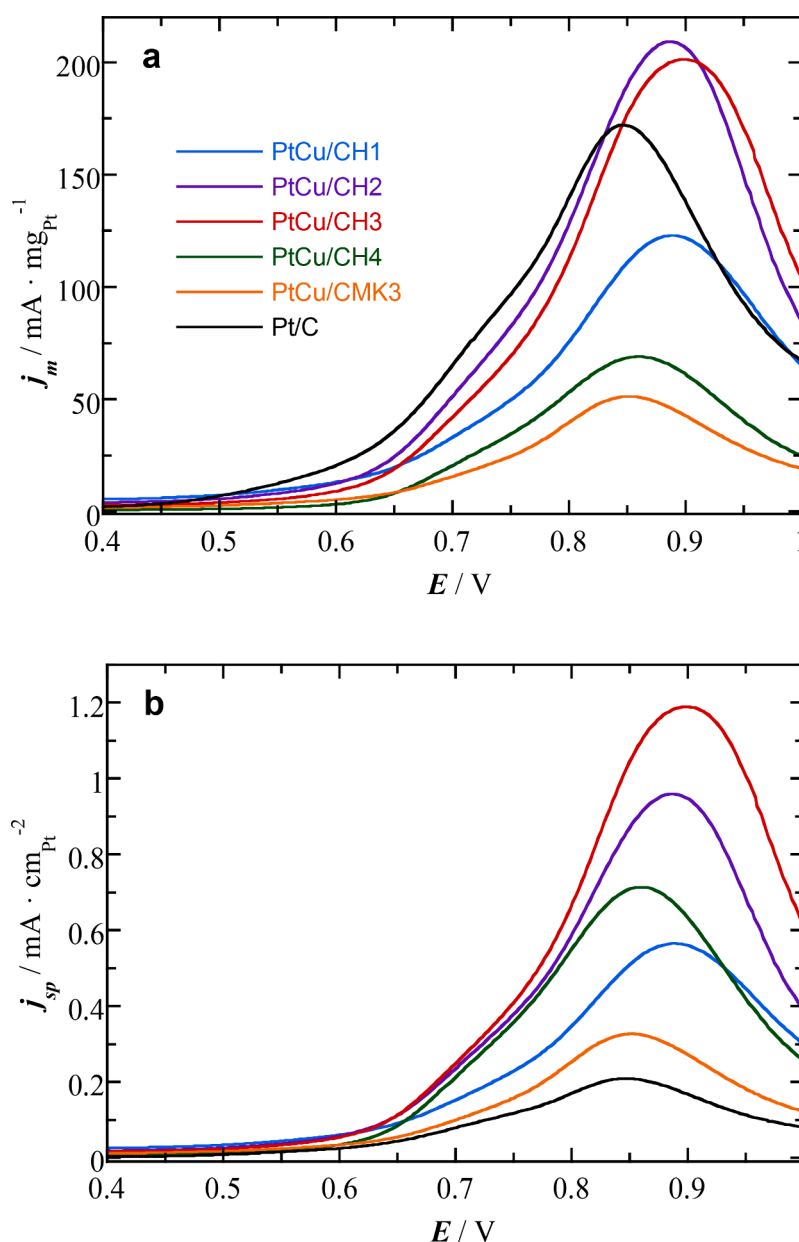
Fig. 9. Direct sweep of the cyclic voltammograms for the MOR in deaerated 1.0 M MeOH + 0.5 M H_2SO_4 solution corresponding to the (a) mass activities (j_m) and (b) specific activities (j_{sp}). Scan rate of 20 mV s^{-1}.

active for the MOR than commercial Pt/C, and there is a progress of activities, attributable, as indicated above, to the different surface structures of the PtCu nanoparticles produced on the different support textures. Note in addition, that the Pt loading of about 20 μg_{Pt} cm^{-2} has been fixed in this work for comparing the activity of the different catalysts. Changing such Pt load could plausibly enhance the obtained results, as shown in previous literature, but this aspect is out of the scope of the present paper [30].

Overall, the electrochemical tests showed that the synthesized PtCu/NMCs were more active than Pt/C in front of the CO stripping, the ORR and the MOR, and this can be attributed to the particular electronic structure of Pt in the PtCu alloy nanoparticles built up during the preparation procedure. There is, however, some dependence of the PtCu/NMC activity on the PtCu alloy nanoparticle composition. This can be due to the formation of different alloy surface structures resulting from the different textural properties of the NMCs, which could condition the transport of the species. The best activity results were obtained with PtCu/CH3, what could be assigned to the best compromise between *meso* and microporosity of CH3 with respect to the other NMCs.

4. Conclusions

PtCu alloy catalysts were supported on chitosan-derived N-doped mesoporous carbons (NMCs), with the double goal of reducing the need of Pt and investigating the viability of inexpensive greener carbons, eventually enhancing the sustainability of low-temperature fuel cells. Carbon supports with differently textural properties were synthesized from easily available chitosan present in disposable biomass, using the cheap silica P20 normally employed for chromatographic separation as hard templating agent. BET specific surface areas over 1000 m^2 g^{-1} were attained, with different mesopore-to-micropore volume ratios. This ratio was 6.1 for the NMC activated with H$_2$SO$_4$ (CH3), exhibiting better textural properties than the ordered mesoporous carbon CMK-3 and Vulcan® XC-72. The nitrogen content of the NMCs ranged between 5.2 and 7.4 wt.% and the XPS results showed about 19% atoms of carbon in C—N bonds, and pyridinic to pyrrolic forms with ratios in the range 40–50%. The Raman analyses indicated the formation of rather defective graphite lattices.

The supported PtCu catalysts for electrochemical tests were prepared sequentially in two steps. The dispersed PtCu nanocrystallites were identified by means of XRD, with compositions in the range 83–90 at.% Pt and mean size between 3.1 and 4.7 nm. The PtCu/NMCs presented CO oxidation peaks placed about 50 mV more negative than commercial Pt/C, thus indicating their higher CO tolerance. The specific activities (current densities relative to the *ECSA*) for the ORR and the MOR were also higher than those of commercial Pt/C and PtCu supported on commercial ordered mesoporous carbon CMK-3, PtCu/CH3 being the most active. The *ECSA* of the PtCu/NMCs was smaller than that of Pt/C and decreased with the microporosity of the NMCs, which was assigned to a higher nanoparticle aggregation, favoured by the microporosity increase. A soft dependence of the crystallite composition with the textural properties of the NMCs was also found, the Pt:Cu at.% ratio being 90:10, with the lowest Cu content, for PtCu/CH3. It is concluded that the compromise between *meso* and microporosity conditioned, through the mass transport of species, the surface structure of the final PtCu nanoparticles on the carbon supports.

Supporting Information (SI) contains 5 figures and 1 table on: TEM micrographs of the synthesized mesoporous carbons; N$_2$ physisorption analyses; Linear sweep voltammograms for the ORR; Cyclic voltammograms for the MOR.

CRediT authorship contribution statement

Julia Garcia-Cardona: Investigation, Formal analysis, Writing – original draft. **Ignasi Sirés:** Validation, Resources, Data curation, Writing – review & editing, Project administration, Funding acquisition.

Marco Mazzucato: Investigation, Formal analysis, Writing – original draft. **Riccardo Brandiele:** Investigation, Formal analysis, Writing – original draft. **Enric Brillas:** Validation, Data curation. **Francisco Alcaide:** Conceptualization, Methodology. **Christian Durante:** Conceptualization, Methodology, Resources, Data curation, Writing – review & editing, Visualization, Supervision, Project administration, Funding acquisition. **Pere L. Cabot:** Conceptualization, Methodology, Resources, Writing – review & editing, Visualization, Supervision, Project administration.

Declaration of Competing Interest

The authors declare that they have no known competing financial interests or personal relationships that could have appeared to influence the work reported in this paper.

Data availability

Data will be made available on request.

Supplementary materials

Supplementary material associated with this article can be found, in the online version, at doi:10.1016/j.electacta.2023.141911.

References

[1] X. Ren, Q. Lv, L. Liu, B. Liu, Y. Wang, A. Liu, G. Wu, Current progress of Pt and Pt-based electrocatalysts used for fuel cells, Sustain. Energy Fuels 4 (2019) 15, https://doi.org/10.1039/c9se00460b.

[2] E.H. Majlan, D. Rohendi, W.R.W. Daud, T. Husaini, M.A. Haque, Electrode for proton exchange membrane fuel cells: a review, Renew. Sustain. Energy Rev. 89 (2018) 117, https://doi.org/10.1016/j.rser.2018.03.007.

[3] A.B. Stambouli, E. Traversa, Fuel cells, an alternative to standard sources of energy, Renew. Sustain. Energy Rev. 6 (2002) 295, https://doi.org/10.1016/S1364-0321(01)00015-6.

[4] E. Antolini, Formation of carbon-supported PtM alloys for low temperature fuel cells: a review, Mater. Chem. Phys. 78 (2003) 563, https://doi.org/10.1016/S0254-0584(02)00389-9.

[5] Z. Liu, X.Y. Ling, X. Su, J.Y. Lee, Carbon-supported Pt and PtRu nanoparticles as catalysts for a direct methanol fuel cell, J. Phys. Chem. B 108 (2004) 8234, https://doi.org/10.1021/jp049422b.

[6] A. Velázquez-Palenzuela, E. Brillas, C. Arias, F. Centellas, J.A. Garrido, R. M. Rodríguez, P.L. Cabot, Structural analysis of carbon-supported Ru-decorated Pt nanoparticles synthesized using forced deposition and catalytic performance toward CO, methanol, and ethanol electro-oxidation, J. Catal. 298 (2013) 112, https://doi.org/10.1016/j.jcat.2012.11.006.

[7] M. Sakthivel, J.F. Drillet, An extensive study about influence of the carbon support morphology on Pt activity and stability for oxygen reduction reaction, Appl. Catal. B 231 (2018) 62, https://doi.org/10.1016/j.apcatb.2018.02.050.

[8] Y. Sung, J. Hwang, J.S. Chung, Characterization and activity correlations of Pt bimetallic catalysts for low temperature fuel cells, Int. J. Hydrogen Energy 36 (2011) 4007, https://doi.org/10.1016/j.ijhydene.2010.12.058.

[9] G. Caballero-Manrique, A. Velázquez-Palenzuela, E. Brillas, F. Centellas, J. A. Garrido, R.M. Rodríguez, P.L. Cabot, Electrochemical synthesis and characterization of carbon-supported Pt and Pt-Ru nanoparticles with Cu cores for CO and methanol oxidation in polymer electrolyte fuel cells, Int. J. Hydrogen Energy 39 (2014) 12859, https://doi.org/10.1016/j.ijhydene.2014.06.089.

[10] K. Jayasayee, J.A.R. Van Veen, T.G. Manivasagam, S. Celebi, E.J.M. Hensen, F. A. de Bruijn, Oxygen reduction reaction (ORR) activity and durability of carbon supported PtM (Co, Ni, Cu) alloys: influence of particle size and non-noble metals, Appl. Catal. B 515 (2012) 111–112, https://doi.org/10.1016/j.apcatb.2011.11.003.

[11] B. Geboes, I. Mintsouli, B. Wouters, J. Georgieva, A. Kakaroglou, S. Sotiropoulos, E. Valova, S. Armyanov, A. Hubin, T. Breugelmans, Surface and electrochemical characterisation of a Pt-Cu/C nano-structured electrocatalyst, prepared by galvanic displacement, Appl. Catal. B 150–151 (2014) 249, https://doi.org/10.1016/j.apcatb.2013.12.020.

[12] J. Georgieva, E. Valova, I. Mintsouli, S. Sotiropoulos, S. Armyanov, A. Kakaroglou, A. Hubin, O. Steenhaut, J. Dille, Carbon-supported Pt(Cu) electrocatalysts for methanol oxidation prepared by Cu electroless deposition and its galvanic replacement by Pt, J. Appl. Electrochem. 44 (2014) 215, https://doi.org/10.1007/s10800-013-0618-2.

[13] J. Maya-Cornejo, R. Carrera-Cerritos, D. Sebastián, J. Ledesma-García, L. G. Arriaga, A.S. Aricò, V. Baglio, PtCu catalyst for the electro-oxidation of ethanol in an alkaline direct alcohol fuel cell, Int. J. Hydrogen Energy 42 (2017) 27919, https://doi.org/10.1016/j.ijhydene.2017.07.226.

[14] A. Sarkar, A. Manthiram, Synthesis of Pt@Cu core-shell nanoparticles by galvanic displacement of Cu by Pt^{4+} ions and their application as electrocatalysts for oxygen reduction reaction in fuel cells, J. Phys. Chem. C 114 (2010) 4725, https://doi.org/10.1021/jp908933r.

[15] E.J. Coleman, A.C. Co, Galvanic displacement of Pt on nanoporous copper: an alternative synthetic route for obtaining robust and reliable oxygen reduction activity, J. Catal. 316 (2014) 191, https://doi.org/10.1016/j.jcat.2014.05.012.

[16] H.Y. Park, J.H. Park, P. Kim, S.J. Yoo, Hollow $PdCu_2@Pt$ core@shell nanoparticles with ordered intermetallic cores as efficient and durable oxygen reduction reaction electrocatalysts, Appl. Catal. B 225 (2018) 84, https://doi.org/10.1016/j.apcatb.2017.11.052.

[17] Y. Zhao, Y. Wu, J. Liu, F. Wang, Dependent relationship between quantitative lattice contraction and enhanced oxygen reduction activity over Pt-Cu alloy catalysts, ACS Appl. Mater. Interfaces 9 (2017) 35740, https://doi.org/10.1021/acsami.7b08437.

[18] J. Garcia-Cardona, I. Sirés, F. Alcaide, E. Brillas, F. Centellas, P.L. Cabot, Electrochemical performance of carbon-supported Pt(Cu) electrocatalysts for low-temperature fuel cells, Int. J. Hydrogen Energy 45 (2020) 20582, https://doi.org/10.1016/j.ijhydene.2020.02.038.

[19] V. Menshchikov, A. Alekseenko, V. Guterman, A. Nechitailov, N. Glebova, A. Tomasov, O. Spiridonova, S. Belenov, N. Zelenina, O. Safronenko, Effective platinum-copper catalysts for methanol oxidation and oxygen reduction in proton-exchange membrane fuel cell, Nanomaterials 10 (2020) 742, https://doi.org/10.3390/nano10040742.

[20] S. Samad, K.S. Loh, W.Y. Wong, T.K. Lee, J. Sunarso, S.T. Chong, W.R.W. Daud, Carbon and non-carbon support materials for platinum-based catalysts in fuel cells, Int. J. Hydrogen Energy 43 (2018) 7823, https://doi.org/10.1016/j.ijhydene.2018.02.154.

[21] E. Antolini, Carbon supports for low-temperature fuel cell catalysts, Appl. Catal. B 88 (2009) 1, https://doi.org/10.1016/j.apcatb.2008.09.030.

[22] A.L. Dicks, The role of carbon in fuel cells, J. Power Sources 156 (2006) 128, https://doi.org/10.1016/j.jpowsour.2006.02.054.

[23] F. Rodríguez-Reinoso, The role of carbon materials in heterogeneous catalysis, Carbon N Y 36 (1998) 159, https://doi.org/10.1016/S0008-6223(97)00173-5.

[24] S. Shahgaldi, J. Hamelin, Improved carbon nanostructures as a novel catalyst support in the cathode side of PEMFC: a critical review, Carbon N Y 94 (2015) 705, https://doi.org/10.1016/j.carbon.2015.07.055.

[25] S. Sharma, B.G. Pollet, Support materials for PEMFC and DMFC electrocatalysts—a review, J. Power Sources 208 (2012) 96, https://doi.org/10.1016/j.jpowsour.2012.02.011.

[26] L.M. Roen, C.H. Paik, T.D. Jarvi, Electrocatalytic corrosion of carbon support in PEMFC cathodes, Electrochem. Solid State Lett. 7 (2004) 8, https://doi.org/10.1149/1.1630412.

[27] Y. Shao, G. Yin, Y. Gao, Understanding and approaches for the durability issues of Pt-based catalysts for PEM fuel cell, J. Power Sources 171 (2007) 558, https://doi.org/10.1016/j.jpowsour.2007.07.004.

[28] M. Enterría, J.L. Figueiredo, Nanostructured mesoporous carbons: tuning texture and surface chemistry, Carbon N Y 108 (2016) 79, https://doi.org/10.1016/j.carbon.2016.06.108.

[29] W. Li, J. Liu, D. Zhao, Mesoporous materials for energy conversion and storage devices, Nat. Rev. Mater. 1 (2016) 16023, https://doi.org/10.1038/natrevmats.2016.23.

[30] S. Güneş, F.Ç. Güldür, Synthesis of OMC supported Pt catalysts and the effect of the metal loading technique on their PEM fuel cell performances, Chem. Eng. Commun. 207 (2020) 961, https://doi.org/10.1080/00986445.2019.1635464.

[31] G. Álvarez, F. Alcaide, O. Miguel, L. Calvillo, M.J. Lázaro, J.J. Quintana, J. C. Calderón, E. Pastor, Technical electrodes catalyzed with PtRu on mesoporous ordered carbons for liquid direct methanol fuel cells, J. Solid State Electrochem. 14 (2010) 1027, https://doi.org/10.1007/s10008-009-0913-3.

[32] J.R.C. Salgado, F. Alcaide, G. Álvarez, L. Calvillo, M.J. Lázaro, E. Pastor, Pt-Ru Electrocatalysts supported on ordered mesoporous carbon for direct methanol fuel cell, J. Power Sources 195 (2010) 4022, https://doi.org/10.1016/j.jpowsour.2010.01.001.

[33] L. Calvillo, M. Gangeri, S. Perathoner, G. Centi, R. Moliner, M.J. Lázaro, Synthesis and performance of platinum supported on ordered mesoporous carbons as catalyst for PEM fuel cells: effect of the surface chemistry of the support, Int. J. Hydrogen Energy 36 (2011) 9805, https://doi.org/10.1016/j.ijhydene.2011.03.023.

[34] G. Gupta, D.A. Slanac, P. Kumar, J.D. Wiggins-Camacho, X. Wang, S. Swinnea, K. L. More, S. Dai, K.J. Stevenson, K.P. Johnston, Highly stable and active Pt-Cu oxygen reduction electrocatalysts based on mesoporous graphitic carbon supports, Chem. Mater. 21 (2009) 4515, https://doi.org/10.1021/cm901203n.

[35] E.P. Ambrosio, C. Francia, M. Manzoli, N. Penazzi, P. Spinelli, Platinum catalyst supported on mesoporous carbon for PEMFC, Int. J. Hydrogen Energy 33 (2008) 3142, https://doi.org/10.1016/j.ijhydene.2008.03.045.

[36] J. Garcia-Cardona, F. Alcaide, E. Brillas, I. Sirés, P.L. Cabot, Testing PtCu nanoparticles supported on highly ordered mesoporous carbons CMK3 and CMK8 as catalysts for low-temperature fuel cells, Catalysts 11 (2021) 724, https://doi.org/10.3390/catal11060724.

[37] X. Long, P. Yin, T. Lei, K. Wang, Z. Zhan, Methanol electro-oxidation on Cu@Pt/C core-shell catalysts derived from Cu MOF, Appl. Catal. B 260 (2020), 118187, https://doi.org/10.1016/j.apcatb.2019.118187.

[38] R. Brandiele, C. Durante, M. Zerbetto, N. Vicentini, T. Kosmala, D. Badocco, P. Pastore, G.A. Rizzi, A.A. Isse, A. Gennaro, Probing the correlation between Pt-support interaction and oxygen reduction reaction activity in mesoporous carbon materials modified with Pt-N active sites, Electrochim. Acta 277 (2018) 287, https://doi.org/10.1016/j.electacta.2018.04.182.

[39] R. Brandiele, F. Poli, L. Picelli, R. Pilot, G.A. Rizzi, F. Soavi, C. Durante, Nitrogen-doped mesoporous carbon electrodes prepared from templating propylamine-functionalized silica, ChemElectroChem 92 (2020) 455, https://doi.org/10.1002/celc.202000098.

[40] R. Brandiele, M. Zerbetto, M.C. Dalconi, G.A. Rizzi, A.A. Isse, C. Durante, A. Gennaro, Mesoporous carbon with different density of thiophenic-like functional groups and their effect on oxygen reduction, ChemSusChem 12 (2019) 4229, https://doi.org/10.1002/cssc.201901568.

[41] R. Brandiele, L. Picelli, R. Pilot, V. Causin, A. Martucci, G.A. Rizzi, A.A. Isse, C. Durante, A. Gennaro, Nitrogen and sulfur doped mesoporous carbons, prepared from templating silica, as interesting material for supercapacitors, ChemistrySelect 2 (2017) 7082, https://doi.org/10.1002/slct.201701404.

[42] G. Daniel, Y. Zhang, S. Lanzalaco, F. Brombin, T. Kosmala, G. Granozzi, A. Wang, E. Brillas, I. Sirés, C. Durante, Chitosan-derived nitrogen-doped carbon electrocatalyst for a sustainable upgrade of oxygen reduction to hydrogen peroxide in UV-assisted electro-Fenton water treatment, ACS Sustain. Chem. Eng. 8 (2020) 14425, https://doi.org/10.1021/acssuschemeng0c04294.

[43] G. Daniel, T. Kosmala, F. Brombin, M. Mazzucato, A. Facchin, M.C. Dalconi, D. Badocco, P. Pastore, G. Granozzi, C. Durante, Highly graphitized Fe-N-C electrocatalysts prepared from chitosan hydrogel frameworks, Catalysts 11 (2021) 390, https://doi.org/10.3390/catal11030390.

[44] H. El Knidri, R. Belaabed, A. Addaou, A. Laajeb, A. Lahsini, Extraction, chemical modification and characterization of chitin and chitosan, Int. J. Biol. Macromol. 120 (2018) 1181, https://doi.org/10.1016/j.ijbiomac.2018.08.139.

[45] J. Solla-Gullón, V. Montiel, A. Aldaz, J. Clavilier, Synthesis and electrochemical decontamination of platinum-palladium nanoparticles prepared by water-in-oil microemulsion, J. Electrochem. Soc. 150 (2003) 104, https://doi.org/10.1149/1.1534600.

[46] A. Sadezky, H. Muckenhuber, H. Grothe, R. Niessner, U. Pöschl, Raman microspectroscopy of soot and related carbonaceous materials: spectral analysis and structural information, Carbon N Y 43 (2005) 1731, https://doi.org/10.1016/j.carbon.2005.02.018.

[47] O. Beyssac, B. Goffé, J.P. Petitet, E. Froigneux, M. Moreau, J.N. Rouzaud, On the characterization of disordered and heterogeneous carbonaceous materials by Raman spectroscopy, Spectrochim. Acta A Mol. Biomol. Spectrosc 59 (2003) 2267, https://doi.org/10.1016/S1386-1425(03)00070-2.

[48] M. Mazzucato, G. Daniel, A. Mehmood, T. Kosmala, G. Granozzi, A. Kucernak, C. Durante, Effects of the induced micro- and meso-porosity on the single site density and turn over frequency of Fe-N-C carbon electrodes for the oxygen reduction reaction, Appl. Catal. B 291 (2021) 120068, https://doi.org/10.1016/j.apcatb.2021.120068.

[49] G. Daniel, M. Mazzucato, R. Brandiele, L. De Lazzari, D. Badocco, P. Pastore, T. Kosmala, G. Granozzi, C. Durante, Sulfur doping versus hierarchical pore structure: the dominating effect on the Fe-N-C site density, activity, and selectivity in oxygen reduction reaction electrocatalysis, ACS Appl. Mater. Interfaces 13 (2021) 42693, https://doi.org/10.1021/acsami.1c09659.

[50] Powder Diffraction File (2018). International Centre for Diffraction Data (ICDD), 12 Campus Boulevard., Newton Square, Pennsylvania 19073-3273, USA.

[51] V.V. Pryadchenko, S.V. Belenov, D.B. Shemet, V.V. Srabionyan, L.A. Avakyan, V. A. Volochaev, A.S. Mikheykin, K.E. Bdoyan, I. Zizak, V.E. Guterman, L.A. Bugaev, Effect of thermal treatment on the atomic structure and electrochemical characteristics of bimetallic PtCu core-shell nanoparticles in PtCu/C electrocatalysts, J. Phys. Chem. C 122 (2018) 17199, https://doi.org/10.1021/acs.jpcc.8b03696.

[52] A.A. Alekseenko, S.V. Belenov, V.S. Menshikov, V.E. Guterman, Pt(Cu)/C electrocatalysts with low platinum content, Russ. J. Electrochem. 54 (2018) 415, https://doi.org/10.1134/S1023193518050026.

[53] J.R. Kitchin, J.K. Nørskov, M.A. Barteau, J.G. Chen, Modification of the surface electronic and chemical properties of Pt(111) by subsurface 3d transition metals, J. Chem. Phys. 120 (2004) 10240, https://doi.org/10.1063/1.1737365.

[54] I. Esparbé, E. Brillas, F. Centellas, J.A. Garrido, R.M. Rodríguez, C. Arias, P. L. Cabot, Structure and electrocatalytic performance of carbon-supported platinum nanoparticles, J. Power Sources 190 (2009) 201, https://doi.org/10.1016/j.jpowsour.2009.01.075.

[55] A. Pavlets, A. Alekseenko, V. Menshchikov, S. Belenov, V. Volochaev, I. Pankov, O. Safronenko, V.E. Guterman, Influence of electrochemical pretreatment conditions of PtCu/C alloy electrocatalyst on its activity, Nanomaterials 11 (2021) 1499, https://doi.org/10.3390/nano11061499.

[56] L. Vega, J. Garcia-Cardona, F. Viñes, P.L. Cabot, K.M. Neyman, Nanostructuring determines poisoning: tailoring CO adsorption on PtCu bimetallic nanoparticles, Mater. Adv. 3 (2022) 4159. 10.1007/s10800-006-9282-0.

[57] Z. Liu, L. Hong, Electrochemical characterization of the electrooxidation of methanol, ethanol and formic acid on Pt/C and PtRu/C electrodes, J. Appl. Electrochem. 37 (2007) 505, https://doi.org/10.1007/s10800-006-9282-0.

[58] A. Hofstead-Duffy, D.J. Chen, S.G. Sun, Y.J. Tong, Origin of the current peak of negative scan in the cyclic voltammetry of methanol electro-oxidation on Pt-based electrocatalysts: a revisit to the current ratio criterion, J. Mater. Chem. 22 (2012) 5205, https://doi.org/10.1039/C2JM15426A.